Airglow imaging observations of small-scale structures driven by convective instability in the upper mesosphere over Tirunelveli (8.7°N)

V. Lakshmi Narayanan,[1] S. Gurubaran,[1] and K. Emperumal[1]

[1] Airglow imaging observations of broadband OH Meinel band emissions made on the night of 20 January 2007 from the tropical Indian site Tirunelveli (8.7°N, 77.8°E) reveal large- and small-scale wave features that are aligned perpendicular to each other and that are associated with gravity wave dynamics. The large-scale waves were the signatures of propagating quasi-monochromatic (QM) waves, whereas the small-scale features were identified to be ripples generated by convective instability in the mesosphere-lower thermosphere (MLT) region. The QM waves showed consistent propagation toward the northwest direction throughout the observation period of ~4.5 hr, whereas the ripples that manifested as short-lived patches in the airglow images were transient and did not show any prominent phase propagation. In addition to these well-resolved structures in images, we infer the presence of waves with relatively longer observed time periods (compared with the observed time period of QM waves) from the spectrum of the time series generated with zenith intensity values derived from the images. From the complementary wind and temperature data obtained with co-located MF radar and Sounding of Atmosphere with Broad band Emission Radiometry on the Thermosphere Ionosphere Mesosphere Energetics and Dynamics mission, an attempt is made to understand the dynamic processes occurring in the vicinity of the mesopause during the night of 20 January 2007. The uniqueness of the present observations is that there were short-lived ripple patches seen in various parts of the sky during the entire observation period of 4.5 hr. The precipitation rates obtained by the Tropical Rainfall Measuring Mission satellite mission suggest that the deep convective activity occurring over the equatorial eastern Indian Ocean provided a plausible source mechanism for sustained generation of the waves observed over Tirunelveli during this night.

1. Introduction

[2] High-frequency gravity waves play a crucial role in the energetics and dynamics of the mesosphere-lower thermosphere (MLT) region [*Fritts and Alexander*, 2003; *McLandress*, 1998]. Most of these waves, having sources in the lower atmosphere, propagate up to and even above the mesosphere with increasing amplitudes. When these waves break or interact with other waves, tides, and background mean wind, the energy and momentum carried by them get deposited in the background environment. The effects brought about by high-frequency waves are pronounced as they carry significant energy density upward. In the past two decades, many observational reports on the characteristics of these ubiquitous waves have been made from the MLT region [*Vincent and Reid*, 1983; *Gavrilov et al.*, 1995; *Taylor et al.*, 1997; *Swenson et al.*, 1999; *Walterscheid et al.*, 1999; *Smith et al.*, 2000; *Suzuki et al.*, 2004; *Wrasse et al.*, 2006]. Even then, the high-frequency gravity waves are not yet well characterized, and their propagation mechanisms are not well understood.

[3] Instability is said to arise when the background conditions of the atmosphere favor an uncontrolled growth of small disturbances [*Chandrasekhar*, 1981]. Such changes in background conditions do occur at the mesospheric heights because of the deposition of energy and momentum by the dynamic processes involving atmospheric gravity waves. Instabilities are thought to play an important role in the cascade of energy from large-scale motions toward smaller scales, leading to turbulence. Our understanding of the characterization and the role played by wave instabilities in the MLT region remains inadequate to date.

---

[1]Equatorial Geophysical Research Laboratory, Indian Institute of Geomagnetism, Krishnapuram, Tirunelveli, India.

[4] Usually, two types of wave-triggered instabilities were observed in the past, namely, dynamic instabilities (or Kelvin-Helmholtz instabilities) and convective instabilities. Dynamic instability is the outcome of extreme shears between adjacent stratified layers. Convective instability results whenever the environmental adiabatic lapse rate is greater than the dry adiabatic lapse rate. In other words, if the potential temperature decreases with height, it results in convective instability, implied by the negative values of the square of the buoyancy frequency. The Richardson number ($R_i = N^2/(du/dz)^2$) is a measure of the stabilizing effect of buoyancy against the destabilizing effect of vertical wind shear between adjacent horizontally stratified layers [*Hecht*, 2004]. The value of the Richardson number is expected to be <0.25 (but greater than zero) for dynamic instabilities and less than zero for convective instabilities [*Beer*, 1974].

[5] Some of the high-frequency small-scale waves and the instabilities that occur in the MLT region are capable of affecting the upper mesospheric chemiluminescent nightglow emissions. Imaging observations of these emissions with all-sky cameras [*Peterson and Kieffaber*, 1973; *Hapgood and Taylor*, 1982] in the past revealed a wealth of information about the small-scale wave motions that are not easy to observe with other techniques. A review of the observational limits of the imagers, radars, and lidars in estimating mesospheric gravity wave parameters was provided by *Gardner and Taylor* [1998].

[6] Many previous studies with airglow imaging [*Taylor et al.*, 1993; *Taylor and Edwards*, 1991; *Frey et al.*, 2000; *Nakamura et al.*, 1998; *Suzuki et al.*, 2004] have shown propagating alternate bright and dark bands that resulted from the passage of high-frequency gravity wave modes. These are referred to as quasi-monochromatic (QM) waves or bands. Their horizontal wavelengths usually lie between 15 and 75 km with apparent phase speeds in the range of 20 to 100 m/s. Any detailed study of dynamic events associated with such waves with supplemental background wind and temperature data, if available, will augment our understanding of the wave dynamical processes and their impact on the environment. Apart from the QM waves, imaging studies (especially with OH Meinel bands) in the past have revealed transient small-scale wavelike fluctuations recognized as ripples, which were shown to arise from in situ generated instabilities [*Nakamura et al.*, 1999; *Hecht*, 2004; *Li et al.*, 2005a, 2005b; *Hecht et al.*, 2005; *Hecht et al.*, 2007]. Their wavelengths were found to be <25 km, and their lifetimes normally do not exceed 45 min. Both convective and dynamical instabilities are capable of generating ripples in airglow images. Previous theoretical and experimental studies [*Fritts and Rastogi*, 1985; *Fritts et al.*, 1997; *Hecht et al.*, 1997; *Yamada et al.*, 2001; *Li et al.*, 2005a, 2005b] have shown that the convectively generated ripples have their phase fronts aligned perpendicularly to those of the gravity wave responsible for the generation of the instability, and the ripples originating from dynamic instabilities have their phase fronts parallel to those of the breaking gravity wave. Once generated, the ripples may rotate and/or advect along with the background wind. Though these small-scale structures are transient, waves that are not strong enough to consistently perturb the airglow emission or are too weak to leave the airglow unaffected may sometimes be seen for a short duration in the airglow images. The small-scale waves that show up in the airglow images need to be carefully examined before categorizing them as ripples or QM waves.

[7] In this work, the results regarding the dynamic events observed in OH Meinel band all-sky airglow images on the night of 20 January 2007 from Tirunelveli are presented and discussed. The supplementary wind and temperature data were obtained from the co-located MF radar and the measurements made by the Sounding of Atmosphere with Broad band Emission Radiometry (SABER) on the Thermosphere Ionosphere Mesosphere Energetics and Dynamics (TIMED) mission, respectively. The airglow images revealed longer propagating band structures and several transient shorter wavelike structures with no appreciable phase motion. The longer band structures were identified as signatures of a propagating QM wave of period of ~15 min, whereas the small-scale structures visible in the airglow images were identified as ripples. Ripples advected horizontally as patches approximately in the direction of the background wind. In addition to these structures, the spectral analysis of time series of zenith intensity values obtained from the images revealed the existence of a spectrum of waves with periods between 18 and 52 min, but we were unable to deduce their propagation direction and appropriate range of phase velocities.

[8] We have made an attempt to understand the underlying processes with the help of the linear theory of atmospheric gravity waves and simple reasoning on the basis of the available knowledge about the generation of convective instabilities. The observations made on 20 January 2007 suggest that the QM wave experienced wave reflection at ~88 km. A sharp temperature gradient was observed with superadiabatic lapse rate occurring at and immediately above this altitude that would have possibly led to the generation of convective instability. The observations also reveal that the shears in the background flow were not strong enough to result in dynamic instability that would have accounted for the observed ripple features. The lifetimes of individual patches of ripples were well within 40 min. These convective ripples were observed to continuously appear and disappear for >4.5 hr, and this implies the existence of a continuous forcing for the waves that would be responsible for the generation of instability at airglow altitudes. Precipitation data sets from the Tropical Rainfall Measuring Mission (TRMM) demonstrate the occurrence of intense deep tropical convection over the eastern Indian Ocean, which was in the direction from which the QM wave came, before and during the period of imaging observations. Because convection is supposed to generate a spectrum of waves, the longer period waves inferred from the spectral analysis of zenith intensity values might have also been generated by convective activity. According to our knowledge, this was the longest duration over which convective ripples were continuously seen in the MLT region. This is the first detailed report on the imaging observations of ripples made from the Indian longitudinal sector.

2. Observations and Data Analysis

[9] All-sky airglow imaging observations were initiated from the low-latitude station, Tirunelveli, on the night of 20 January 2007. About 4.5 hr of data were collected during that night between 1845 UT (0015 Indian Standard Time (IST)) and 2315 UT (0445 IST) with OH filter and a background
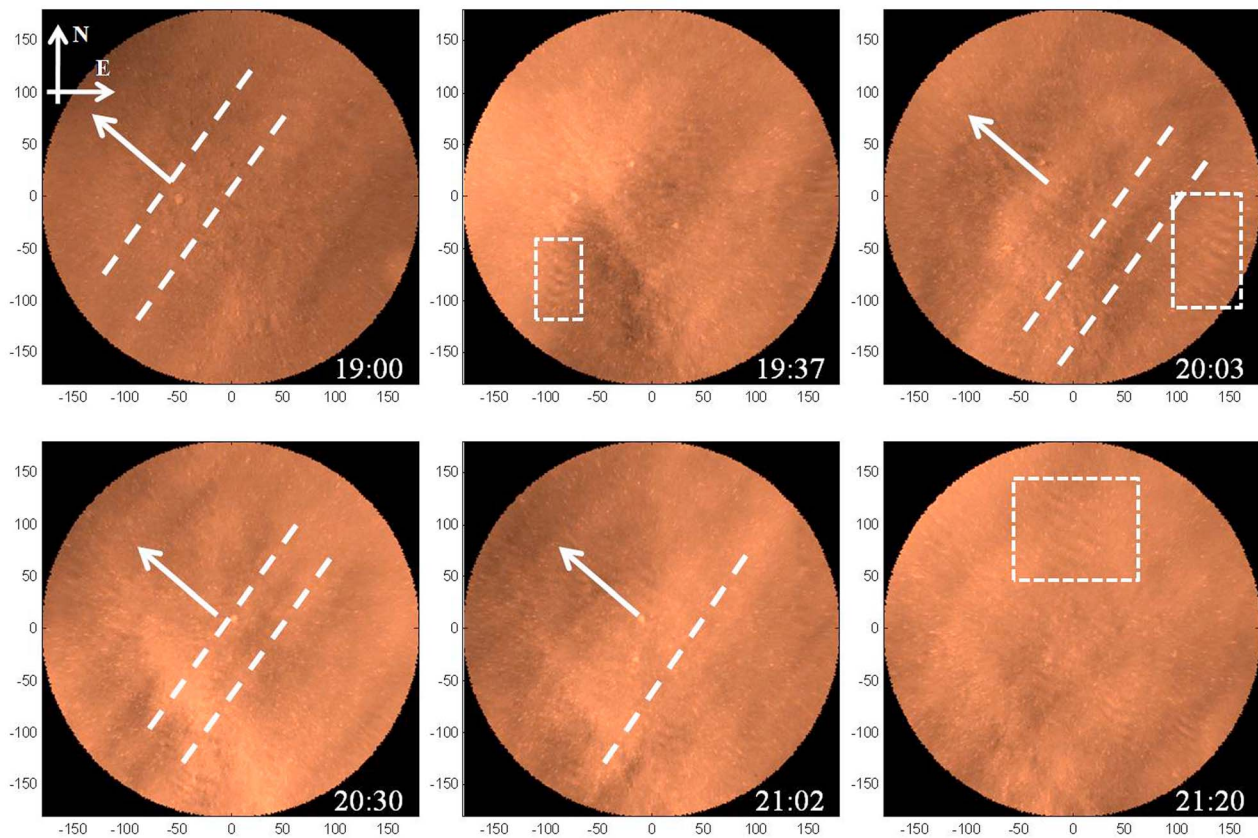
Figure 1. All sky OH nightglow images (false-colored) showing bands and ripples. Times of the images are given in UT. The *x*- and *y*-axes represent distance in kilometers.

filter centered at 572.3 nm. The OH filter was a broadband filter covering the Meinel band emissions between the wavelengths 705.3 and 928.2 nm with a notch at 865 nm to suppress the $O_2(0,1)$ band emission. The images were captured with a back illuminated CCD of 512×512-pixel array. During the experiment, an exposure time of 2 min was given to acquire an OH airglow image. Regions of images inside a field of view of 130° were used for analysis, which covered ~360 km at 87 km altitude, the centroid height of the OH emission. The instrument details and the method of image analysis are described by *Narayanan et al.* [2009b]. In brief, the acquired OH images were flat-fielded with the average of star removed background images. An average of those flat-fielded images obtained over 1 hr duration was then subtracted from the individual flat-fielded images. This enhances the clarity of wavelike perturbations noticed in raw images. Finally, the image was projected on a grid with equidistant points based on the method discussed by *Garcia et al.* [1997]. With this instrument, imaging observations of a mesospheric bore event from Tirunelveli were reported earlier [*Narayanan et al.*, 2009a].

[10] On the night of 20 January 2007, transient small-scale wavelike features (that we identify later as ripples) were observed along with larger bandlike features for >4.5 hr as depicted in Figure 1. Figure 2 shows the enlarged view of the squared regions in Figure 1, wherein the small-scale features are well displayed. The large-scale band structures were seen to propagate toward the northwest at an azimuth of 309° covering the entire field of view. Though the contrast of these

bands in individual images is less, they are well displayed if a sequence of images is seen in motion. The crests of shorter wavelike features with wavelengths ranging from 5 to 13 km were aligned approximately perpendicular to the band feature. They did not show prominent phase propagation. Rather, they advected in patches toward the direction that was approximately opposite to that of the propagation of the large-scale band structures. Later it is shown that the advection was along the direction of the background wind.

[11] Because the data were mostly collected with an OH filter on this night, we generated time series of zenith intensity values by taking average of 13×13 pixels from the center of the flat-fielded images corresponding to the zenith of the observation location. The wave fluctuations affecting the nightglow emissions were superposed on the nocturnal variation as shown in Figure 3a. The observed intensities were first interpolated at 1 min time intervals and were then subjected to a 35-point smoothing to approximately remove the nocturnal variation. In Figure 3a, the dots represent averages observed from flat-fielded images, the dotted line represents the interpolated curve, and the continuous line represents the 35-point smoothing. In Figure 3b, we show the fluctuations present after removal of the nocturnal variation. Figure 3c depicts the amplitude fast Fourier transform spectrum of data presented in Figure 3b. The spectrum shows peaks in the time period range from 18 to 52 min.

[12] The background wind information was obtained from the co-located MF radar data. The radar system probes the mesospheric altitude region of 68 to 98 km at 2 km height
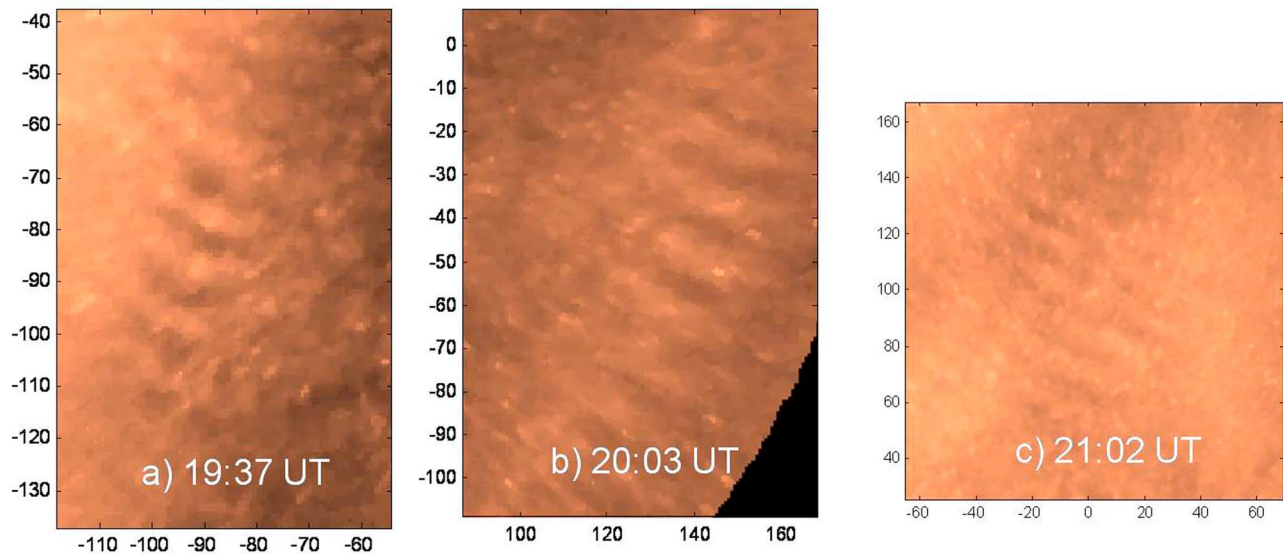
Figure 2. Enlarged view of the squared regions in Figure 1 highlighting a few of the ripple features.

intervals, though with a vertical resolution of ~4 km and at 2 min time intervals. Further details of the radar operation are provided in *Rajaram and Gurubaran* [1998]. Because MF radar wind measurements suffer from frequent data gaps, we adopted the criterion that at least 25% of the data should be available every hour for further analysis. This limits the height region to 84–98 km that passed this criterion. For this work, the radar data were used to obtain true horizontal wind, the wind component along the direction of propagation of the observed airglow band structures, and the vertical wind shear between 84 and 88 km. The radar data quality is not good enough to detect short-period waves that were observed in imaging observations. The analysis did not reveal any longer-period (a few to several hours) gravity waves in the radar-observed winds.

[13] We used temperature data obtained by the SABER instrument onboard TIMED mission that made snapshot temperature measurements over two nearby locations with geographic coordinates (10.4°N, 70.6°E) and (7.0°N, 71.2°E) at respective times of 1947:44 UT and 1948:44 UT on 20 January 2007. The measurements were sampled at every 0.4 km altitude. Because the true vertical resolution of the instrument was ~2 km, we estimated temperature values at every 1 km height interval by taking 2 km sliding averages. The schematic in Figure 4 shows the ground observation site and the locations corresponding to the SABER measurements. The plots of both temperature measurements are shown in Figure 5 along with their average. As can be noted in Figure 5, the two temperature profiles correlate well, especially up to 93 km. It may also be noted that the latitude of the ground observation site, 8.7°N, is midway between the latitudes of the SABER measurements (10.4°N and 7.0°N), and the imager had coverage up to these latitudes. For the present analysis, we assume that there was negligible longitudinal variation in the temperature between SABER measurement locations and the ground observation site. This would thus imply that the average of the two SABER temperature profiles would fairly represent the background temperature over the imager location. In Figure 6, we depict

the plots of OH 1.6 μm emission height profiles obtained from the SABER data sets. The satellite-derived OH emission profiles confirm that the peak OH emission altitude was ~86 km at these times.

[14] To trace the possible source of the observed gravity waves, we examined 3-hourly precipitation data obtained from the NASA archive of TRMM data sets. The data product version used in this work is 3B42, which provides rainfall rate in a 0.25° × 0.25° geographical grid. Precipitation rates are a good proxy for deep tropical convective activity, which is currently thought to be an important source of mesospheric gravity waves in the tropical region [*Walterscheid et al.*, 1999; *Nakamura et al.*, 2003]. The rainfall maps analyzed in this work reveal strong convective activity before and during the course of the event in the direction southeast of the observation site as discussed later.

3. Results and Discussion

[15] The presence of a band feature observed for >4 hr during the night of 20 January 2007 indicates that it might be the signature of an intense QM gravity wave propagating through the probing region throughout the period. The average horizontal wavelength, λ_h, of the observed bands is estimated to be 42.9 ± 4.3 km with an apparent phase speed, c, of 47.7 ± 4.8 m/s. This yields an observed time period of ~15 ± 3 min. This is in accordance with the peaks noticed in the zenith intensity values in the period range 14–19 min.

[16] To obtain phase velocities and direction of propagation of the relatively longer-period waves inferred from spectral analysis of zenith intensity values (see Figure 3), we also made averages of 13 × 13 pixels for the north-east, north-west, south-east, and south-west directions surrounding the zenith. The centers for those averages were displaced by a spacing of 54 pixels horizontally and vertically from the center of the zenith square. All the time series showed the presence of fluctuations in the same time period range as observed for zenith. But we could not decipher any phase lag in cross-correlation analysis between them (not shown).
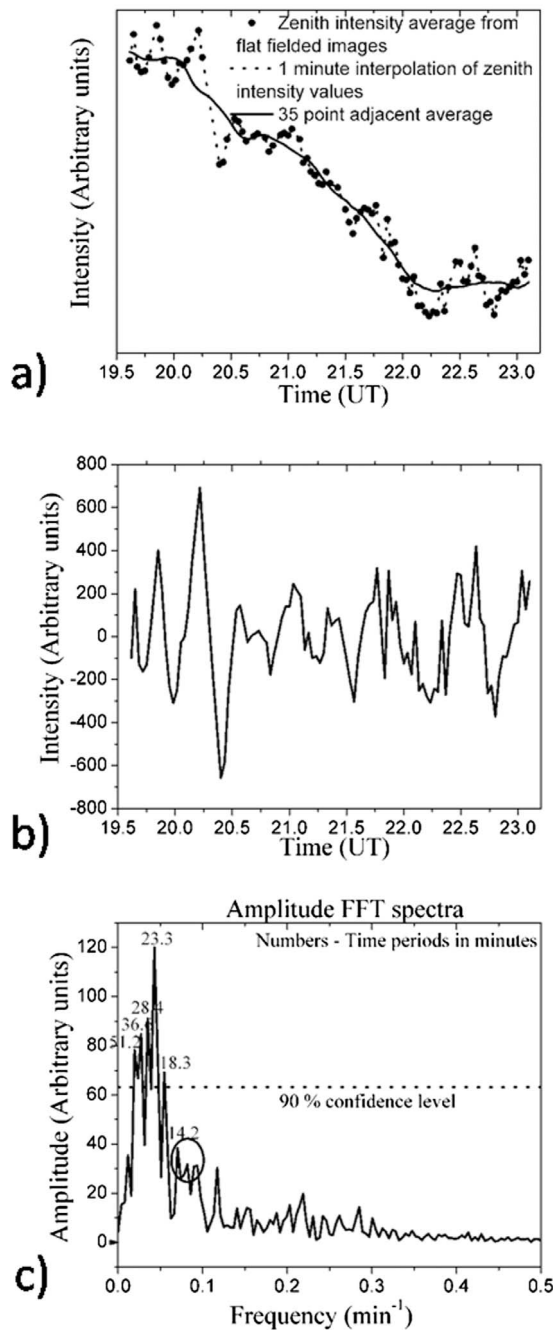
Figure 3. (a) Average of 13 × 13 pixels near the zenith of imaging region are represented by dots, their one minute interpolation by dotted line, and 35-point smoothing representing nocturnal secular variation by continuous line. (b) Detrended data after removal of nocturnal secular variation. (c) Amplitude fast Fourier transform spectra of the detrended data.

Hence, we are unable to identify their propagation direction and apparent phase velocities. The fact that the relatively longer-period waves were not well resolved in images is an indication that their horizontal wavelengths might have been of the order of a few hundred kilometers beyond the region covered by the field of view of the instrument.
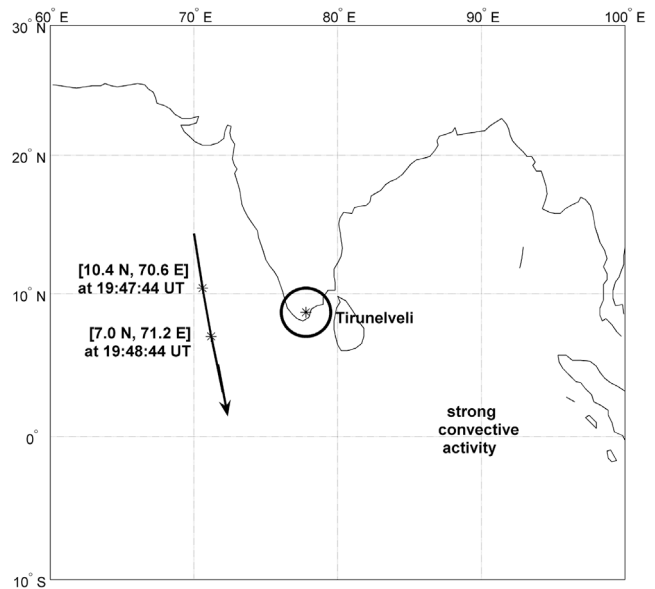

Figure 4. A schematic map showing the ground observation site and two nearby locations corresponding to Sounding of Atmosphere with Broad band Emission Radiometry (SABER) observations.

[17] To obtain the vertical wave numbers of the QM wave at the OH emission heights, we used the following dispersion relation:

$$m^2 = \frac{N^2}{(u-c)^2} - \frac{u_{zz}}{(u-c)} + \frac{1}{H}\frac{u_z}{(u-c)} - \frac{1}{4H^2} - k^2, \quad (1)$$

where k and m are the horizontal and vertical wave numbers, respectively, N is the buoyancy frequency, c is the apparent phase speed observed in the image data, u is the background wind speed in the direction of propagation of the wave, u_z and
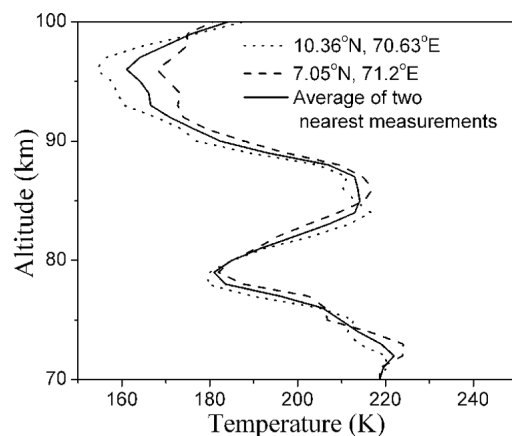

Figure 5. Temperature profiles obtained by the SABER instrument onboard Thermosphere Ionosphere Mesosphere Energetics and Dynamics (TIMED) mission corresponding to the locations (10.4°N, 70.63°E) and (7.05°N, 71.2°E). The average temperature profile derived from the SABER measurements is also shown.
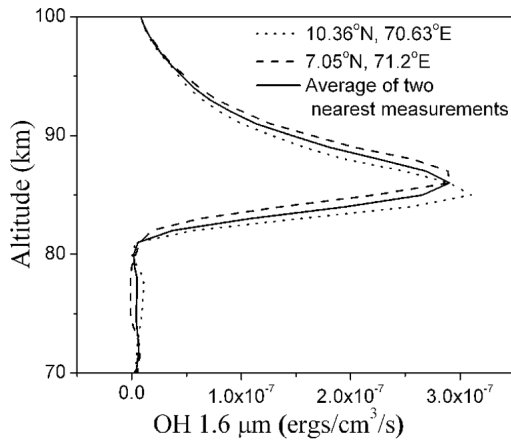
Figure 6. Same legend as Figure 5 but for the OH emission profiles.

u_{zz} are the first and second derivatives of u with height z, respectively, and H is the scale height (taken as 6.4 km). Equation (1) is a well-known form of the gravity wave dispersion relation derived from linear theory, which includes the effects of varying background wind. Only compression effects, which are supposed to be very small, were neglected in arriving at equation (1).

[18] From the acquired images, the wave parameters of the QM wave, namely, the horizontal wavelength, λ_h, and the apparent phase speed, c, were estimated. The height profile of the time-averaged (for the period 1830–2030 UT) wind along the direction of the wave propagation is shown in Figure 7, with the error bars representing the standard deviations of individual measurements made within the chosen hours. Though MF radar winds were available at 2 km vertical spacing, we used linearly interpolated wind values at every 1 km height intervals for the calculations. Results for the calculated wave parameters along with background conditions are given in Table 1 for every 1 km altitude from 85 to 93 km. The true wind polar plot in Figure 8 shows that the wind flow was nearly opposite to the direction of wave propagation. This plot depicts the wind vector points of individual measurements between 1830 and 2030 UT in the height region of 84 to 90 km. The average magnitude of the true wind between 1830 and 2030 UT was 57 m/s directed at an azimuth of 143°. We have also calculated the average magnitude and direction of true wind for the 5 hr (1830–2330 UT) spanning the entire imaging observation and found the values to be 47 m/s and 139° for true wind speed and azimuth, respectively, which were only slightly different from the 2 hr average values. The background wind condition did not change much, especially with regard to its direction, during the entire observation period. Thus, we think that the 2 hr we considered here as representing the background conditions suffice to examine the processes at work during this night. It may be noted that these 2 hr were centered on the SABER temperature observations.

[19] Apart from the QM wave, patches of several smaller structures were observed in the airglow images with a variety of wavelengths ranging from 5 to 13 km. In general, they did not show any prominent and consistent phase propagation, though individual structures as a whole drifted approximately

toward the southeast. The normal to their phase fronts were seen to lie within the azimuths of 25° to 55°. Noteworthy is the fact that the true wind was blowing toward the southeast (Figure 8). The lifetime of the individual patches was usually <20 min and never >40 min. Previous observations of ripples [*Hecht*, 2004; *Hecht et al.*, 1997; *Li et al.*, 2005b] have shown that transient convectively generated ripple phase fronts are oriented approximately perpendicular to the breaking gravity wave fronts and that the ripples drift or advect along with the background mean flow.

[20] The altitude profiles of the square of buoyancy frequency and the potential temperature computed for the night of 20 January 2007 are shown in Figure 9. At heights just below 90 km, N^2 was negative and the atmosphere was convectively unstable as inferred from the potential temperature profile that is seen to attain a negative gradient. This lends credence to our assertion that the small-scale wavelike features observed over Tirunelveli were ripples generated by convective instability.

[21] To test whether any strong shears in the mesosphere generated dynamic instabilities that would have resulted in the observed small-scale structures, we next examined wind shears between 84 and 88 km altitudes from the 10 min averages of zonal and meridional winds derived from MF radar observations (not shown). The maximum wind shear was found to be ~25 m/s/km in the meridional direction at 1955 UT on the night of 20 January 2007. Zonal winds did not show any significant shear during the period of observations. In spite of the presence of significant wind shears, it is shown below that the conditions were still not favorable for the generation of dynamic instabilities.

[22] The nondimensional Richardson number, which is an indicator for dynamic instability, was calculated from the 85 to 93 km height region at every 1 km interval. The values are given in Figure 10. At none of the heights was the Richardson number in the range 0–0.25 so that the shear instability could result in ripples or billows. At this point, it may be noted that the radar would not be able to detect any shear in the wind occurring within ~4 km, which is the height resolution of the
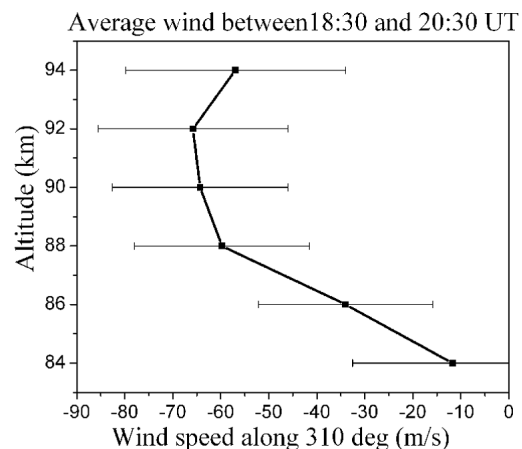

Figure 7. Average of MF radar wind measurements from 1830 to 2030 UT along 310°, which is the wave propagation direction. The error bars indicate the standard deviation. Note that the wind velocity values were negative, indicating wind flow opposite to that of wave propagation.

**Table 1.** Calculated Wave Parameters Between 85 and 93 km Altitudes

Height (km)	u (m/s)	T (K)	H (m)	$N^2 \times 10^{-4}$ (rad^2/s^2)	m^2 (1/km^2)	λ_z (km)	Wave Period(s)	Buoyancy Period(s)	θ_w (deg)
85	−22.9	214.2	6449	4.386	0.084	21.6	607	300	60.4
86	−34.0	213.7	6435	3.978	0.033	34.4	524	315	53.1
87	−46.9	213.0	6414	2.749	0.024	40.3	453	379	33.3
88	−59.8	207.0	6233	−0.201	0.080	22.2	399	-	-
89	−62.1	193.1	5816	−1.396	−0.037	-	391	-	-
90	−64.3	182.4	5491	0.596	−0.009	-	383	814	-
91	−65.1	176.4	5313	2.018	−0.013	-	380	442	-
92	−65.8	170.8	5144	2.535	0.031	35.7	378	395	-
93	−61.4	166.5	5015	4.095	−0.005	-	393	310	37.8

instrument. It is fairly reasonable to assume that those shears at scales smaller than the radar height resolution would not have persisted for >4 hr considering that the largest wind shears at scales detectable by the radar did not persist more than a few tens of minutes. With this reasoning, we may then rule out the possibility of dynamic instability producing ripples for duration of ~4.5 hr as observed in the present study. Rather, the observations reported in this work (imager data revealing the perpendicular orientation of ripple phase fronts with respect to the gravity wave phase fronts and the SABER temperature profiles demonstrating a convectively unstable region at airglow emitting altitudes) support convective instability as a plausible source for the observed ripple events. As a further affirmation, we notice that the ripple phase fronts were aligned in the direction of the background wind flow at an azimuth of 150° ± 15°, in conformity with earlier reports of convective ripples [e.g., *Li et al.*, 2005b].

[23] When the background mean flow is along the wave propagation direction and its speed nears the apparent phase speed of the wave, the wave is expected to impart its momentum and energy to the mean flow, thereby accelerating it. On the other hand, when the mean flow direction is opposite to the direction of the phase propagation of the wave, the wave period would get Doppler-shifted toward the buoyancy period favoring wave reflection [e.g., *Hines and Reddy*, 1967; *Robinson*, 1997]. Gravity wave reflection may be total or partial. In the case of total reflection, the

incident wave energy completely gets reflected back, whereas in the case of partial reflection a part of the energy traverses into the evanescent region accounting for some reflection loss. If the thickness of the evanescent region above the level of reflection is z, then the energy lost by the wave in tunneling through the region is inversely proportional to the product, mz [*Hecht et al.*, 2001b]. Because the energy carried by the evanescent wave decreases exponentially, the wave will not effectively tunnel if the evanescent region is thicker than the vertical wavelength of the wave. Only a few experimental studies on the processes governing the reflection of gravity waves have been reported [e.g., *Wust and Bittner*, 2008; *Collins and Smith*, 2004].

[24] The QM wave observed over Tirunelveli during the night of 20 January 2007 did encounter a situation described above, and we infer that the wave was nearing a level of reflection ~88 km. Below that altitude, from the plot of temperatures in Figure 5, it can be seen that there was a temperature inversion of 32 K between the 79 and 84 km altitudes. In Figure 10, the calculated buoyancy time period, T_b, and the wave intrinsic period, T_w, are plotted. The small-scale high-frequency waves tend to reflect when $T_w = T_b$ [*Beer*, 1974; *Robinson*, 1997]. This can easily be understood once we realize that the buoyancy period is nothing but the characteristic time period of oscillation for an air parcel displaced vertically in a stably stratified atmosphere. All the other wave frequencies can be assumed as those resulting from oscillation about a plane inclined to the horizontal. If the
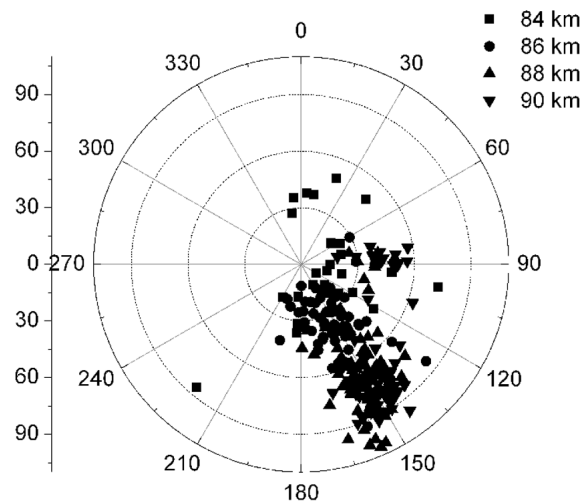
Figure 8. True wind scatter plot of wind measurements made during 1830–2030 UT in the altitude region of 84–90 km.
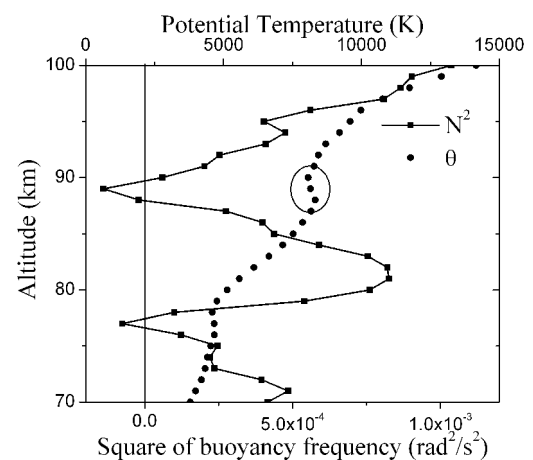
Figure 9. Altitude profiles of potential temperature (θ) and square of buoyancy frequency (N^2). Notable features are the decrease in potential temperature illustrated by a circle and the negative values of N^2 at those corresponding heights.
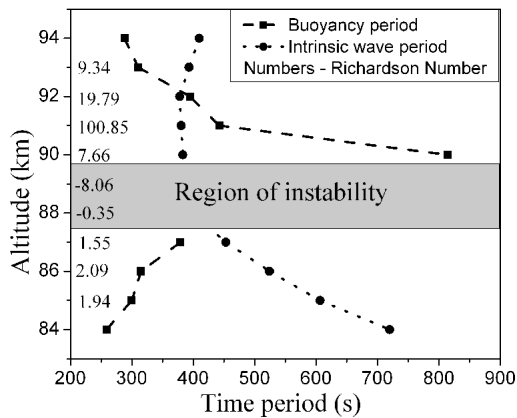
Figure 10. Height profiles of intrinsic wave period and buoyancy period. The numbers in the inner left of y axis are the calculated Richardson numbers.

oscillations become more and more vertical, the plane about which the transverse oscillations occur becomes more and more horizontal. In that scenario, gravity waves become horizontally propagating with a wave angle of 0° as their intrinsic frequency approaches the buoyancy frequency. The wave angle is the angle made by the wave normal with the horizontal. As the time period of the wave approaches that of the buoyancy period, we may expect the wave angle to decrease as shown in Table 1.

[25] Also, from Figure 10 and Table 1, one can see that the intrinsic time period of the QM wave under consideration was nearing that of the buoyancy time period at ~88 km leading to the wave reflection. It can also be noted from Table 1 that around this level, m^2 attained negative values, thus clearly indicating wave reflection. The condition for wave reflection is m^2 going from positive to negative values, indicating the wave becoming evanescent. It may be noted that the SABER observations do reveal a superadiabatic temperature lapse rate of 10.2 K/km between 87 and 90 km.

[26] The instability region occurring at and immediately above the level of reflection of the observed QM wave suggests a possible relationship between wave reflection and instability, leading to generation of ripples. It is not clear whether the instability causes the wave to reflect or whether the process of wave reflection seeds the instabilities. If the instability drives wave reflection, the perpendicular orientation of the wave fronts with ripples requires an explanation, unless it was a coincidence, because in such a case, similar waves propagating in other directions should also undergo reflection. Thus, in the scenario of instability seeding the wave reflection, the instability should be the outcome of other dynamic processes such as the interaction between other waves observed in spectral analysis, for example. In the latter case of wave reflection seeding the instability features, it is possible that the energy transmitted into the evanescent region pushes the atmosphere from a marginally stable to an unstable state. No quantification of amount of wave energy that could enter the evanescent region is made here, however, to establish this link between wave reflection and the onset of instability. The usual method of estimating individual QM wave energy fluxes from OH imaging requires the wave to traverse the entire OH layer [*Swenson and Liu*, 1998;

Swenson and Gardner, 1998; *Swenson et al.*, 1999; *Swenson et al.*, 2000]. In this case, the QM wave encounters a level of reflection near the peak of OH emission layer itself, and hence such an estimate will not be a correct one. At this point, we would like to point out that such orthogonal orientation of phase fronts of a strong evanescent QM wave and ripples has been reported earlier in the work of *Hecht et al.* [2007]. Also, the short-scale QM wave observed in OH emissions along with ripples reported by *Hecht et al.* [1997] were not accompanied by similar features at O_2 emission heights indicating the wave breaking or overturning within OH and O_2 emission heights.

[27] The repeated generation and disappearance of ripples in different parts of the sky for ~4.5 hr indicates that the atmosphere was repeatedly forced to an unstable state at ~88 km as soon as it became marginally stable. Furthermore, the discrete patchy appearance of ripples indicates localized formation of instabilities. The disappearance of ripples signifies the energy cascade to smaller scales ultimately restoring stability to the region.

[28] An observation similar to this in some sense but for a shorter duration was studied by *Hecht et al.* [1997]. Along with the simulation study by *Fritts et al.* [1997], they suggested that an observed gravity wave of a 4 to 6 hour period made the atmosphere marginally stable while the short-period gravity wave (observed as a QM wave) forced it to an unstable state. In the present observations of 20 January 2007, the relatively longer period (23–50 min) waves inferred from the time series of zenith intensity values might have been responsible for bringing the atmosphere close to an unstable state. Gravity waves with periods greater than a few hours were not observed over the present location around this time.

[29] Usually, the instability features occurring in the atmosphere occur over a relatively thin altitude extent. Earlier simulation studies by *Fritts et al.* [1997] suggested that the wavelength of the convectively generated ripples will be twice that of the thickness of the instability region. However, observational studies of *Hecht et al.* [1997, 2001a] found the convective ripple wavelengths to be more than three times the thickness of the instability region. In the present work, we infer the thickness of the instability region to be ~2 km from SABER observations (refer to Table 1). The ratio of the ripple wavelength to the depth of the instability region would then lie in the range 2–6.

[30] For the ripples to have repeatedly formed for such a long duration, we anticipate that the gravity wave responsible for the ripple events should have continuous forcing for >4.5 hr. This required a temporally sustained source for the generation of the QM wave under consideration.

[31] Deep convective activity is thought to be an important source of high-frequency gravity waves, especially in the tropics [*Swenson and Espy*, 1995; *Nakamura et al.*, 2003; *Brown et al.*, 2004; *Medeiros et al.*, 2004; *Hecht et al.*, 2004; *Snively and Pasko*, 2008]. Several modeling efforts were made in the recent past to identify the mechanisms by which gravity waves are generated during convective activity [*Fovell et al.*, 1992; *Alexander et al.*, 1995; *Vadas and Fritts*, 2001; *Lane et al.*, 2001; *Walterscheid et al.*, 2001; *Song et al.*, 2003; *Alexander et al.*, 2004; *Vadas et al.*, 2009].

[32] To examine the role of deep tropical convective events, if any, in the generation of the observed QM wave, we used the 3-hourly precipitation data from the NASA archive
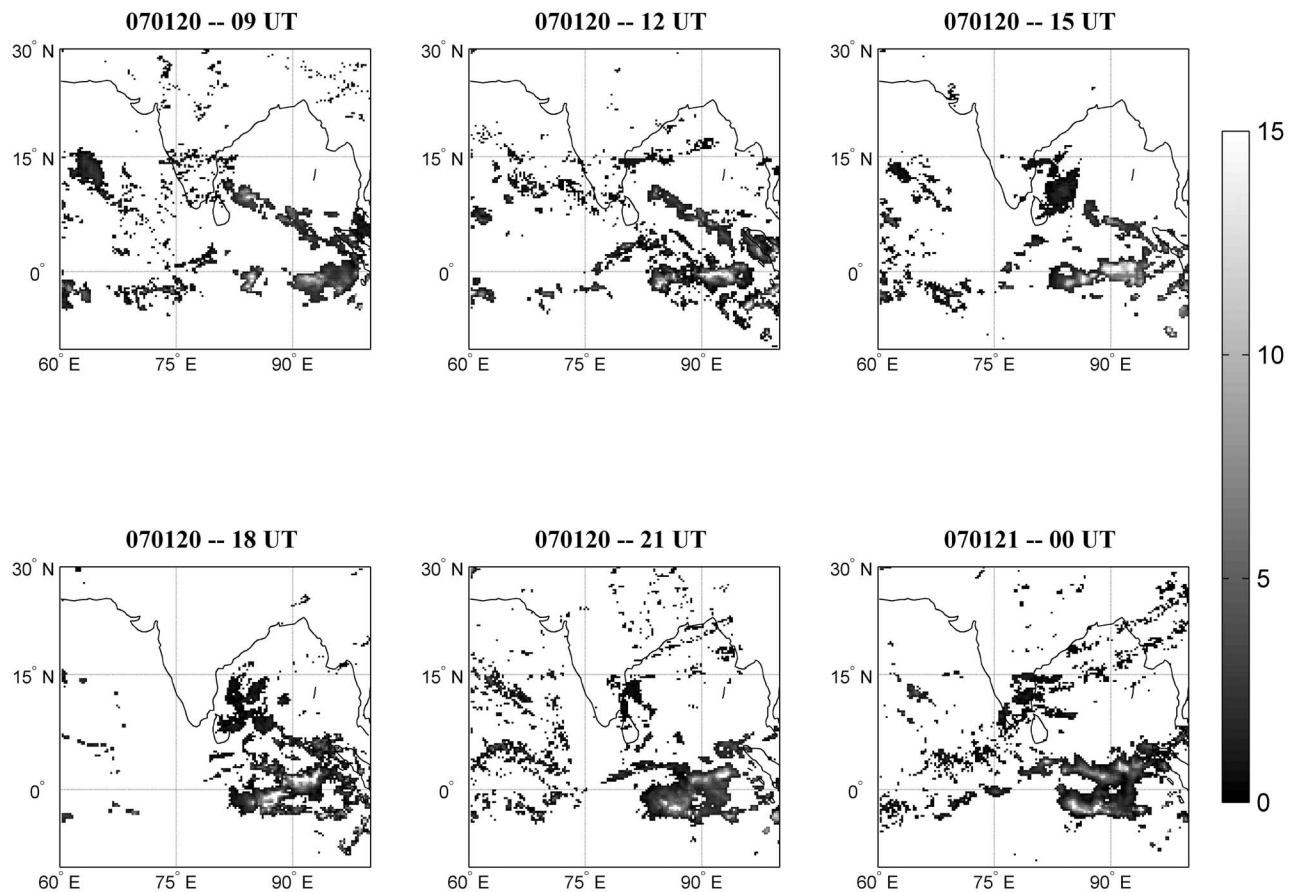
Figure 11. TRMM precipitation maps derived from 3-hourly precipitation data (mm/hr) for successive three hr from 0900 UT on 20 January to 0000 UT on 21 January 2007.

of the TRMM. The TRMM precipitation rates are considered a good proxy for deep tropical convective activity. In Figure 11, we depict the precipitation maps derived from the 3-hourly TRMM data for the period 0900 to 2400 UT on 20 January 2007. Figure 11 shows that strong convection with precipitation rates >15 mm/hr occurred at 1200 UT, several hours before the observation of ripples, in the tropical region southeast of the ground observation site, and persisted until the end of optical observation at Tirunelveli. We suggest that the sustained convective activity occurring in the southeast of the imaging site might have been responsible for the generation of the waves observed in imaging. Ray tracing analyses for the QM wave may confirm this connection.

4. Summary and Conclusions

[33] In this case study, we have presented results from the concurrent observation of bands and ripples on the night of 20 January 2007 made from the low-latitude Indian site Tirunelveli. This was the first observation of ripples at mesospheric altitudes from the Indian sector and to our knowledge the longest duration of ripple observations using an all-sky airglow imager. The ripples were continuously appearing and disappearing in different parts of the sky within the field of view. We summarize below our perspective of the sequence of events that might have led to the generation of ripples over Tirunelveli.

[34] On 20 January 2007, intense convective activity took place with high precipitation occurring over the equator directed southeast of the observation site. At upper mesospheric altitudes, the all-sky airglow imager observations revealed a prominent QM gravity wave mode, possibly generated as a result of deep convective activity. The wave with a horizontal wavelength of ~43 km propagated toward the northwest at an apparent phase speed of ~48 m/s at airglow-emitting altitudes. The analysis revealed that the QM wave experienced reflection near 88 km when the background wind was blowing in a direction opposite to that of wave propagation. In addition to the QM wave, preliminary spectral analysis of zenith intensity time series shows the presence of longer-period waves with periodicities between 23 and 50 min. The occurrence of reflection and instability features at the same height region along with the perpendicular orientation of the QM wave and ripple phase fronts indicates a possible relationship between them. Here, we propose that the atmosphere was driven close to an unstable state, probably by relatively longer-period waves as those inferred from zenith intensity time series. The energy of QM wave transmitted into the evanescent part during reflection might have driven the atmosphere into instability. It is likely that this process repeated as soon as the ripples disappeared and the atmosphere regained marginal stability. Moreover, the ripple features had their phase fronts aligned along the

background wind direction, and they appeared to drift with the mean flow, all of which are in conformity with the earlier observations of ripples driven by convective instability. Our observations and analysis suggest that the convective ripple wavelengths were in a range from two to six times the depth of the instability region.

References

Alexander, M. J., J. R. Holton, and D. R. Durran (1995), The gravity wave response above deep convection in a squall line simulation, *J. Atmos. Sci.*, *52*, 2212–2226.

Alexander, M. J., P. T. May, and J. H. Beres (2004), Gravity waves generated by convection in the Darwin area during the Darwin Area Wave Experiment, *J. Geophys. Res.*, *109*, D20S04, doi:10.1029/2004JD004729.

Beer, T. (1974), *Atmospheric Waves*, Wiley, New York.

Brown, L. B., A. J. Gerrard, J. W. Meriwether, and J. J. Makela (2004), All-sky imaging observations of mesospheric fronts in OI 557.7 nm and broadband OH airglow emissions: Analysis of frontal structure, atmospheric background conditions, and potential sourcing mechanisms, *J. Geophys. Res.*, *109*, D19104, doi:10.1029/2003JD004223.

Chandrasekhar, S. (1981), *Hydrodynamic and Hydromagnetic Stability*, Dover Publications, New York.

Collins, R. L., and R. W. Smith (2004), Evidence of damping and overturning of gravity waves in the arctic mesosphere: Na lidar and OH temperature observations, *J. Atmos. Solar-Terr. Phys.*, *66*, 867–879.

Fovell, R., D. Durran, and J. R. Holton (1992), Numerical simulation of convectively generated stratospheric gravity waves, *J. Atmos. Sci.*, *49*, 1427–1442.

Frey, H. U., S. B. Mende, J. F. Arens, P. R. McCullough, and G. R. Swenson (2000), Atmospheric gravity wave signatures in the infrared hydroxyl OH airglow, *Geophys. Res. Lett.*, *27*(1), 41–44, doi:10.1029/1999GL010695.

Fritts, D. C., and M. J. Alexander (2003), Gravity wave dynamics and effects in the middle atmosphere, *Rev. Geophys.*, *41*(1), 1003, doi:10.1029/2001RG000106.

Fritts, D. C., and P. K. Rastogi (1985), Convective and dynamical instabilities due to gravity wave motions in the lower and middle atmosphere: Theory and observations, *Radio Sci.*, *20*(6), 1247–1277, doi:10.1029/RS020i006p01247.

Fritts, D. C., J. R. Isler, J. H. Hecht, R. L. Walterscheid, and Ø. Andreassen (1997), Wave breaking signatures in sodium densities and OH nightglow 2. Simulation of wave and instability structures, *J. Geophys. Res.*, *102*(D6), 6669–6684, doi:10.1029/96JD01902.

Garcia, F. J., M. J. Taylor, and M. C. Kelly (1997), Two-dimensional spectral analysis of mesospheric airglow image data, *Appl. Opt.*, *36*, 7374–7385.

Gardner, C. S., and M. J. Taylor (1998), Observational limits for lidar, radar, and airglow imager measurements of gravity wave parameters, *J. Geophys. Res.*, *103*(D6), 6427–6437, doi:10.1029/97JD03378.

Gavrilov, N. M., A. H. Manson, and C. E. Meek (1995), Climatological monthly characteristics of middle atmospheric gravity waves (10 min– 10 h) during 1979–1993 at Saskatoon, *Ann. Geophys.*, *13*, 285–295.

Hapgood, M. A., and M. J. Taylor (1982), Analysis of airglow image data, *Ann. Geophys.*, *38*, 805–813.

Hecht, J. H. (2004), Instability layers and airglow imaging, *Rev. Geophys.*, *42*, RG1001, doi:10.1029/2003RG000131.

Hecht, J. H., R. L. Walterscheid, and R. A. Vincent (2001a), Airglow observations of dynamical (wind shear-induced) instabilities over Adelaide, Australia, associated with atmospheric gravity waves, *J. Geophys. Res.*, *106*(D22), 28,189–28,197, doi:10.1029/2001JD000419.

Hecht, J. H., A. Z. Liu, R. L. Walterscheid, and R. J. Rudy (2005), Maui Mesosphere and Lower Thermosphere (Maui MALT) observations of the evolution of Kelvin-Helmholtz billows formed near 86 km altitude, *J. Geophys. Res.*, *110*, D09S10, doi:10.1029/2003JD003908.

Hecht, J. H., R. L. Walterscheid, M. P. Hickey, and S. J. Franke (2001b), Climatology and modeling of quasi-monochromatic atmospheric gravity waves observed over Urbana Illinois, *J. Geophys. Res.*, *106*(D6), 5181–5195, doi:10.1029/2000JD900722.

Hecht, J. H., S. Kovalam, P. T. May, G. Mills, R. A. Vincent, R. L. Walterscheid, and J. Woithe (2004), Airglow imager observations of atmospheric gravity waves at Alice Springs and Adelaide, Australia during the Darwin Area Wave Experiment (DAWEX), *J. Geophys. Res.*, *109*, D20S05, doi:10.1029/2004JD004697.

Hecht, J. H., A. Z. Liu, R. L. Walterscheid, S. J. Franke, R. J. Rudy, M. J. Taylor, and P.-D. Pautet (2007), Characteristics of short-period wavelike features near 87 km altitude from airglow and lidar observations over Maui, *J. Geophys. Res.*, *112*, D16101, doi:10.1029/2006JD008148.

Hecht, J. H., R. L. Walterscheid, D. C. Fritts, J. R. Isler, D. C. Senft, C. S. Gardner, and S. J. Franke (1997), Wave breaking signatures in OH airglow and sodium densities and temperatures 1. Airglow imaging, Na lidar, and MF radar observations, *J. Geophys. Res.*, *102*(D6), 6655–6668, doi:10.1029/96JD02619.

Hines, C. O., and C. A. Reddy (1967), On the propagation of atmospheric gravity waves through regions of wind shear, *J. Geophys. Res.*, *72*(3), 1015–1034, doi:10.1029/JZ072i003p01015.

Lane, T. P., M. J. Reeder, and T. L. Clark (2001), Numerical modeling of gravity wave generation by deep tropical convection, *J. Atmos. Sci.*, *58*, 1249–1274.

Li, F., A. Z. Liu, G. R. Swenson, J. H. Hecht, and W. A. Robinson (2005a), Observations of gravity wave breakdown into ripples associated with dynamical instabilities, *J. Geophys. Res.*, *110*, D09S11, doi:10.1029/2004JD004849.

Li, T., C.-Y. She, B. P. Williams, T. Yuan, R. L. Collins, L. M. Kieffaber, and A. W. Peterson (2005b), Concurrent OH imager and sodium temperature/wind lidar observation of localized ripples over northern Colorado, *J. Geophys. Res.*, *110*, D13110, doi:10.1029/2004JD004885.

McLandress, C. (1998), On the importance of gravity waves in the middle atmosphere and their parameterization in general circulation models, *J. Atmos. Solar-Terr. Phys.*, *60*, 1357–1383.

Medeiros, A. F., H. Takahashi, P. P. Batista, D. Gobbi, and M. J. Taylor (2004), Observations of atmospheric gravity waves using airglow all-sky CCD imager at Cachoeira Paulista, Brazil (23°S, 45°W), *Geofisica Int.*, *43*, 29–39.

Nakamura, T., T. Aono, T. Tsuda, A. G. Admiranto, E. Achmad, and Suranto (2003), Mesospheric gravity waves over a tropical convective region observed by OH airglow imaging in Indonesia, *Geophys. Res. Lett.*, *30*(17), 1882, doi:10.1029/2003GL017619.

Nakamura, T., A. Higashikawa, T. Tsuda, and Y. Matsushita (1999), Seasonal variations of gravity wave structures in OH airglow with a CCD imager at Shigaraki, *Earth Planets Space*, *51*, 897–906.

Nakamura, T., T. Tsuda, H. Miyagawa, Y. Matsushita, H. Fukunishi, Y. Takahashi, and Y. Yamada (1998), Propagation directions of gravity wave patterns observed in OH CCD images during the SEEK Campaign, *Geophys. Res. Lett.*, *25*(11), 1793–1796, doi:10.1029/98GL01064.

Narayanan, V. L., S. Gurubaran, and K. Emperumal (2009a), A case study of a mesospheric bore event observed with an all-sky airglow imager at Tirunelveli (8.7°N), *J. Geophys. Res.*, *114*, D08114, doi:10.1029/2008JD010602.

Narayanan, V. L., S. Gurubaran, and K. Emperumal (2009b), Imaging observations of upper mesospheric nightglow emissions from Tirunelveli (8.7°N), *Indian J. Radio Space Phys.*, *38*, 150–158.

Peterson, A. W., and L. M. Kieffaber (1973), Infrared photography of OH airglow structures, *Nature*, *242*, 321–322.

Rajaram, R., and S. Gurubaran (1998), Seasonal variabilities of low-latitude mesospheric winds, *Ann. Geophys.*, *16*, 197–204.

Robinson, T. R. (1997), Nonlinear reflection of internal gravity waves by thermospheric winds, *Adv. Space Res.*, *20*, 1261–1264.

Smith, S. M., M. Mendillo, J. Baumgardner, and R. R. Clark (2000), Mesospheric gravity wave imaging at a subauroral site: First results from Millstone Hill, *J. Geophys. Res.*, *105*(A12), 27,119–27,130, doi:10.1029/1999JA000343.

Snively, J. B., and V. P. Pasko (2008), Excitation of ducted gravity waves in the lower thermosphere by tropospheric sources, *J. Geophys. Res.*, *113*, A06303, doi:10.1029/2007JA012693.

Song, I.-S., H.-Y. Chun, and T. P. Lane (2003), Generation mechanisms of convectively forced internal gravity waves and their propagation to the stratosphere, *J. Atmos. Sci.*, *60*, 1960–1980.

Suzuki, S., K. Shiokawa, Y. Otsuka, T. Ogawa, and P. Wilkinson (2004), Statistical characteristics of gravity waves observed by an all-sky imager at Darwin, Australia, *J. Geophys. Res.*, *109*, D20S07, doi:10.1029/2003JD004336.

Swenson, G. R., and P. J. Espy (1995), Observations of 2-dimensional airglow structure and Na density from the ALOHA, October 9, 1993 "storm flight", *Geophys. Res. Lett.*, *22*(20), 2845–2848, doi:10.1029/95GL02795.

Swenson, G. R., and A. Z. Liu (1998), A model for calculating acoustic gravity wave energy and momentum flux in the mesosphere from OH airglow, *Geophys. Res. Lett.*, *25*(4), 477–480, doi:10.1029/98GL00132.

Swenson, G. R., and C. S. Gardner (1998), Analytical models for the responses of the mesospheric OH* and Na layers to atmospheric gravity waves, *J. Geophys. Res.*, *103*(D6), 6271–6294, doi:10.1029/97JD02985.

Swenson, G. R., R. Haque, W. Yang, and C. S. Gardner (1999), Momentum and energy fluxes of monochromatic gravity waves observed by an OH imager at Starfire Optical Range, New Mexico, *J. Geophys. Res.*, *104*(D6), 6067–6080, doi:10.1029/1998JD200080.

Swenson, G. R., M. J. Alexander, and R. Haque (2000), Dispersion imposed limits on atmospheric gravity waves in the mesosphere: Observations from OH airglow, *Geophys. Res. Lett.*, *27*(6), 875–878, doi:10.1029/1999GL010738.

Taylor, M. J., and R. Edwards (1991), Observations of short period mesospheric wave patterns: In situ or tropospheric wave generation?, *Geophys. Res. Lett.*, *18*(7), 1337–1340, doi:10.1029/91GL01516.

Taylor, M. J., E. H. Ryan, T. F. Tuan, and R. Edwards (1993), Evidence of preferential directions for gravity wave propagation due to wind filtering in the middle atmosphere, *J. Geophys. Res.*, *98*(A4), 6047–6057, doi:10.1029/92JA02604.

Taylor, M. J., W. R. Pendleton Jr., S. Clark, H. Takahashi, D. Gobbi, and R. A. Goldberg (1997), Image measurements of short-period gravity waves at equatorial latitudes, *J. Geophys. Res.*, *102*(D22), 26,283–26,299, doi:10.1029/96JD03515.

Vadas, S. L., and D. C. Fritts (2001), Gravity wave radiation and mean responses to local body forces in the atmosphere, *J. Atmos. Sci.*, *58*, 2249–2279.

Vadas, S. L., J. Yue, C.-Y. She, P. A. Stamus, and A. Z. Liu (2009), A model study of the effects of winds on concentric rings of gravity waves from a convective plume near Fort Collins on 11 May 2004, *J. Geophys. Res.*, *114*, D06103, doi:10.1029/2008JD010753.

Vincent, R. A., and I. M. Reid (1983), HF Doppler measurements of mesospheric gravity wave momentum fluxes, *J. Atmos. Sci.*, *40*(5), 1321–1333.

Walterscheid, R. L., G. Schubert, and D. G. Brinkman (2001), Small-scale gravity waves in the upper mesosphere and lower thermosphere generated by deep tropical convection, *J. Geophys. Res.*, *106*(D23), 31,825–31,832, doi:10.1029/2000JD000131.

Walterscheid, R. L., J. H. Hecht, R. A. Vincent, I. M. Reid, J. Woithe, and M. P. Hickey (1999), Analysis and interpretation of airglow and radar observations of quasi-monochromatic gravity waves in the upper mesosphere and lower thermosphere over Adelaide, Australia (35°S, 138°E), *J. Atmos. Sol. Terr. Phys.*, *61*, 461–478.

Wrasse, C. M., et al. (2006), Mesospheric gravity waves observed near equatorial and low-middle latitude stations: wave characteristics and reverse ray tracing results, *Ann. Geophys.*, *24*, 3229–3240.

Wust, S., and M. Bittner (2008), Gravity wave reflection: Case study based on rocket data, *J. Atmos. Sol. Terr. Phys.*, *70*, 742–755.

Yamada, Y., H. Fukunishi, T. Nakamura, and T. Tsuda (2001), Breaking of small-scale gravity wave and transition to turbulence observed in OH airglow, *Geophys. Res. Lett.*, *28*(11), 2153–2156, doi:10.1029/2000GL011945.

K. Emperumal, S. Gurubaran, and V. Lakshmi Narayanan, Equatorial Geophysical Research Laboratory, Indian Institute of Geomagnetism, Krishnapuram, Tirunelveli 627 011, India. (gurubara@iigs.iigm.res.in)